Journal of Mines, Metals and Fuels, *71(12): 2493-2511; 2023. DOI: 10.18311/jmmf/2023/36129*

Print ISSN : 0022-2755

Journal of Mines, Metals and Fuels

Contents available at: *www.informaticsjournals.com/index.php/jmmf*

Numerical Investigation of Flow Hydrodynamics in a Flow Field and Porous Substrate Configuration for Redox Flow Battery Application

Rakesh Basavegowda Krishnappa[1,3]*, S. Gowreesh Subramanya[2,3] and Abhijit Deshpande[4]

[1]*Department of Mechanical Engineering, Jyothy Institute of Technology, Bengaluru - 560082, Karnataka, India; rakeshgowda36@gmail.com*

[2]*Department of Mechanical Engineering, JSS Academy of Technical Education, Bengaluru - 560060, Karnataka, India*

[3]*Visvesvaraya Technological University, Belagavi - 590018, Karnataka, India*

[4]*Domain Expert, Powertrain CFD, Mercedes-Benz RD India, Bengaluru-560066, Karnataka, India*

Abstract

In the recent past, most of the literature reported that the electrolyte circulations in parallel flow field configurations exhibit severe non-uniformity with higher Pressure Drop (Δp). The present work proposes a three-dimensional computational design of flow field configurations to achieve a single-phase uniform flow with minimal pump power and flow dispersion over an active cell area of 131cm2 for All Iron Redox Flow Battery (AIRFB). Computational investigation of the Pressure Drop (Δp), electrolyte flow velocity and uniform flow distribution in the channels and through the graphite felt electrode under various flow conditions was conducted using the Computational Fluid Dynamics (CFD) tool. It is observed from the results that the Multi-Channel Serpentine Flow Field (MCSFF) has the least pressure drop among the other flow fields. However, the Cross-Split Serpentine Flow Field (CSSFF) resulted in better flow circulation and dispersion over the entire active cell area with a high uniformity index, operating at a wide range of flow rates with a reasonable Pressure Drop (Δp). The porous media permeability and a strong function of Compression Ratio (CR) were numerically validated from the well-known correlation existing in the literature. At CR 50% it was observed that the volume uniformity index of the felt was 69%, which would correspondingly enhance the rate of mass transfer and electro-kinetics at electrode felt and ion conductivity across the membrane. The CSSFF configuration is predominant in terms of uniform flow distribution and wettability at the defined operating conditions resulting in enhanced cell performance.

Keywords: *All Iron Redox Flow Battery, Compression Ratio, Computational Fluid Dynamics, Cross-Split Serpentine Flow Field, Permeability, Pressure Drop, Uniformity Index*

1.0 Introduction

The current worldwide electric energy generation capacity is about 20 terawatt per hour, where more than 70% of the electrical energy is contributed by non-renewable energy sources and less than 10% from intermittent renewable sources. The energy demand is expected to double in the coming years. Environmental concerns, resource constraints and energy security concerns have led the way to harnessing energy from clean, green, safe and reliable sources. The Energy Storage System (ESS) can be installed to store and retrieve renewable energy at the grid level, to

**Author for correspondence*

enable its stability and reliability to improve the delivery and efficiency of the grid[1,2]. In the recent past several distinct energy storage technologies such as circulating hydro, compressed air, electrochemical, thermal, flywheel[3] etc. have been developed. Among these technologies, Redox Flow Batteries (RFBs) have proven their stance in the electrochemical energy storage segment offering the perfect combination of efficiency, rapid sensitivity, scalability, long lifecycle, low maintenance cost, flexibility, least impact on the environment and a promising storage system especially for renewable energy at medium and large-scale application with a reasonably flexible system design[4]. RFB being a safer alternative to the Li-ion stationary system, complies with local legislation on fire safety. Standardisation has progressed through the International Electrochemical Commission, in addition to upgraded grid storage standards[5]. The commercially viable existing combination of Sodium/Sulfur (Na/S) battery technology for moderate-scale grid applications has progressed with producing more than 300 Mega Watts of discharge power capacity[6]. Many research and development activities are emerging in full swing starting from the different cell designs, construction, cell features, techniques for electrode characterisation and reaction environment to best suit the operating condition to enhance the cell performance[7]. The redox flow cell concept has been around for nearly 4 decades, with the initial development of vanadium redox flow battery[8].

Few studies on electrode intrusion effect on pressure drop and electrochemical performance at different flow channel configurations, and permeability, subjected to varying compression ratios were conducted and measured over different active cell areas for an all-vanadium redox flow battery. The increased pressure gradient across a cell domain may lead to electrolyte flow mal-distribution, causing high mass transfer polarisations[9-13].

Experimental and numerical hydrodynamic studies were conducted to investigate and understand the different serpentine flow fields, flow characteristics, their effects and where alternative approaches were applied to improve the overall cell performance[14-19]. Pressure Drop () losses occur through the flow channels, inter junctions of pipes, cell stack, and along the stack-storage reservoirs to be regulated and controlled. Higher flow rates would increase energy capacity, but consume higher pump power in turn reduces the cell stack efficiency[20,21]. The flow characteristic and uniformity analysis significantly help to design optimal flow frames to improve uniformity parameters, and variability range coefficient[22]. The electrochemical performance characteristics for several variant interdigitated flow fields have shown flow maldistribution over an active cell area and serpentine flow fields have shown better results among the existing design[23]. A couple of research articles reported that the performance study of the RFB and fuel cell application resulted in a 5% increase in energy efficiency with the presence of the serpentine flow field for a range of operating conditions[24]. A bend loss coefficient is an explicit factor of Pressure Drop (and a function of curvature ratio, aspect ratios and channel spacer lengths[25]. RFBs with the serpentine flow field are the significant configuration for uniform flow distribution and reactant penetration through porous substrate[26].

A review of RFB on less discussed aspects of flow field design is expected to reduce the polarisation, pressure losses, novel stack design for high energy density storage, discharge power density and to minimise shunt currents. A uniform flow distribution, localised potential and current distribution directly reflect on the utilisation of electrolyte reactants and the active surface area of porous electrode[27]. The design optimisation of the flow field can add to reducing the overall set-up cost incurred for RFB[28]. Mass transport polarisation is one of the crucial parameters for improving uniform flow distribution, and varying mass transport at a high State of Charge (SOC) and High Current Density (HCD) would essentially enhance the performance of the cell[29].

Most of the literature reported that different performance parameters such as flow field design configuration, electrode characterisation and electrolytes operating on a wide range of conditions, had improved the performance of flow cell battery storage systems. Yet there exists an ample opportunity to optimise these parameters on experimental and modeling approaches.

This RFB system had a range of applications at the off-grid level and also served as an auxiliary power unit, which stores and retrieves renewable energy which is intermittent, more effective for a longer duration and cost-effective too. This system application is used in prominent industries such as mining, petrochemical and automobile production plants etc. The mining and mineral processing industry is one of the most energy-intensive industries worldwide, where power consumption accounts for up to 40% of the mine's total operating budget. Demand for raw materials increases as the world population grows as well, and growth in mineral demand, combined with falling mineral ore grade, is likely to increase the industry's energy demand across certain activities such as exploration, extraction, beneficiation and processing, and refining. The mine sites due to their remoteness, are faced with climatic and distance-related challenges concerning supplied energy, including the dependency on a limited-grid, still mine operations, substantially depend on fossil fuels as a main energy source like diesel, heavy oils, and coal etc. which greatly impact on the environmental ecosystem. The Global Mining Initiative (GMI) and Industry Framework for Sustainable Development (IFSD) brought together the world's largest mining, metals and minerals companies to focus on Sustainable Development (SD) and key issues of energy and greenhouse gas emissions due to concerns over climate change impacts. Environmental Management System (EMS) and Life Cycle Assessment (LCA) practices, would implement the concept of cleaner production in the mining industry through renewable sources. For instance, Advanced Explorations Inc. is investigating alternative energy sources for future iron ore operations located in Nunavut, Canada, because these sources are cleaner and could reduce operating costs (The Globe and Mail, 2012). Paraszczak and Fytas provided several examples of mining operations where renewable energy sources were integrated to reduce carbon emissions and eventually enhance the public's perspective of the industry. This research work addresses the challenges associated with storing and retrieving renewable energy using an Energy Storage System (ESS) which is an IRFB system, for a longer duration efficiently, with low operating cost per kw at an off-grid level, and also provides constant, consistent and cleaner energy for seamless operations at mining sites[30-33]. Iron is also an abundantly available and eco-friendly element

As per literature reviews the Serpentine Flow Field (SFF) is a promising flow configuration over other flow fields. Efforts have been made to numerically analyse the hydrodynamic behaviour of modified versions of SFF along with porous electrodes using a well-known Tamayol-Bahrami model for correlation[34]. The computational validations were performed to study and analyse the operating parameters, i.e., Pressure Drop across the flow channel, electrode plane regions, permeability and the flow uniformity, and electrolyte dispersion through the porous electrode, which would enhance the mass transfer potential, and improve the cell electrochemical activity.

2.0 Methodology

The systematic assembly of an IRFB cell is depicted in Figure 1. The main components of IRFB are bipolar plates with flow channels with inlet and outlet, electrodes, anionic membrane, electrolyte, copper current collectors, gaskets and end plates.

The chemical reactions in the battery are given by Equations (1), (2), (3)[35].

Positive electrode:

$$2Fe^{2+} \leftrightarrow 2Fe^{3+} + 2e^- \quad E^0 = 0.77 \text{ V} \tag{1}$$

Negative electrode:

$$Fe^{2+} + 2e^- \leftrightarrow Fe^0 \quad E^0 = -0.44 \text{ V} \tag{2}$$

Overall:

$$3Fe^{2+} \leftrightarrow Fe^0 + 2Fe^{3+} \quad E^0 = 1.21\text{V} \tag{3}$$

IRFB system, which has an ideal power density and current capacity integrates more cells to form a stack. During the operation, an electrolyte is constantly circulated using a peristaltic pump through the bipolar plates flow channel of respective cells from the storage tank. System performance evaluation is based on the energy density, depth of discharge, columbic, voltaic and energy efficiency.

3.0 Computational Fluid Dynamics Model

The model constitutes two half-cell regions, one for the positive and the other for the negative half, each cell integrated with electrode and flow field domain. Flow fields are grooved with channels. Reactant activity is higher in the positive electrolyte than in the negative electrolyte[36]. Mass transport phenomenon can be well

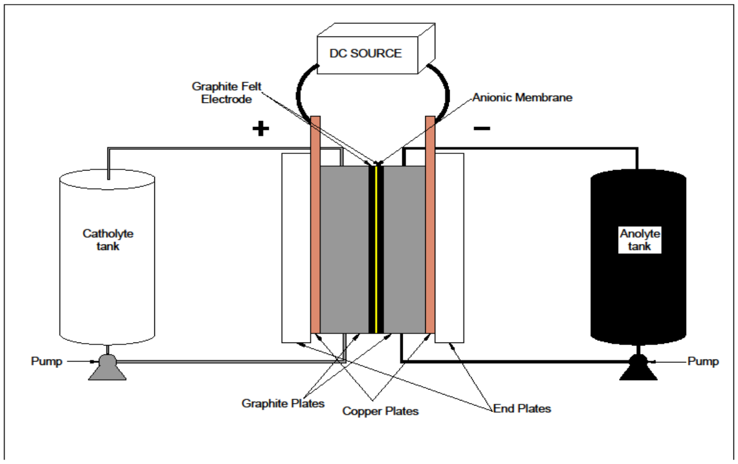

Figure 1. A systematic assembly of an iron redox flow battery.

established and controlled with optimal flow design. This paper reports different flow field configuration models such as Single Channel Serpentine Flow Field (SCSFF), Multi-Channel Serpentine Flow Field (MCSFF) and Cross-Split Serpentine Flow Field (CSSFF) These are developed using Solid Works Premium 2018 SP 4.0 developed by Dassault Systems as shown in Figure 2.

3.1 Flow Field Models

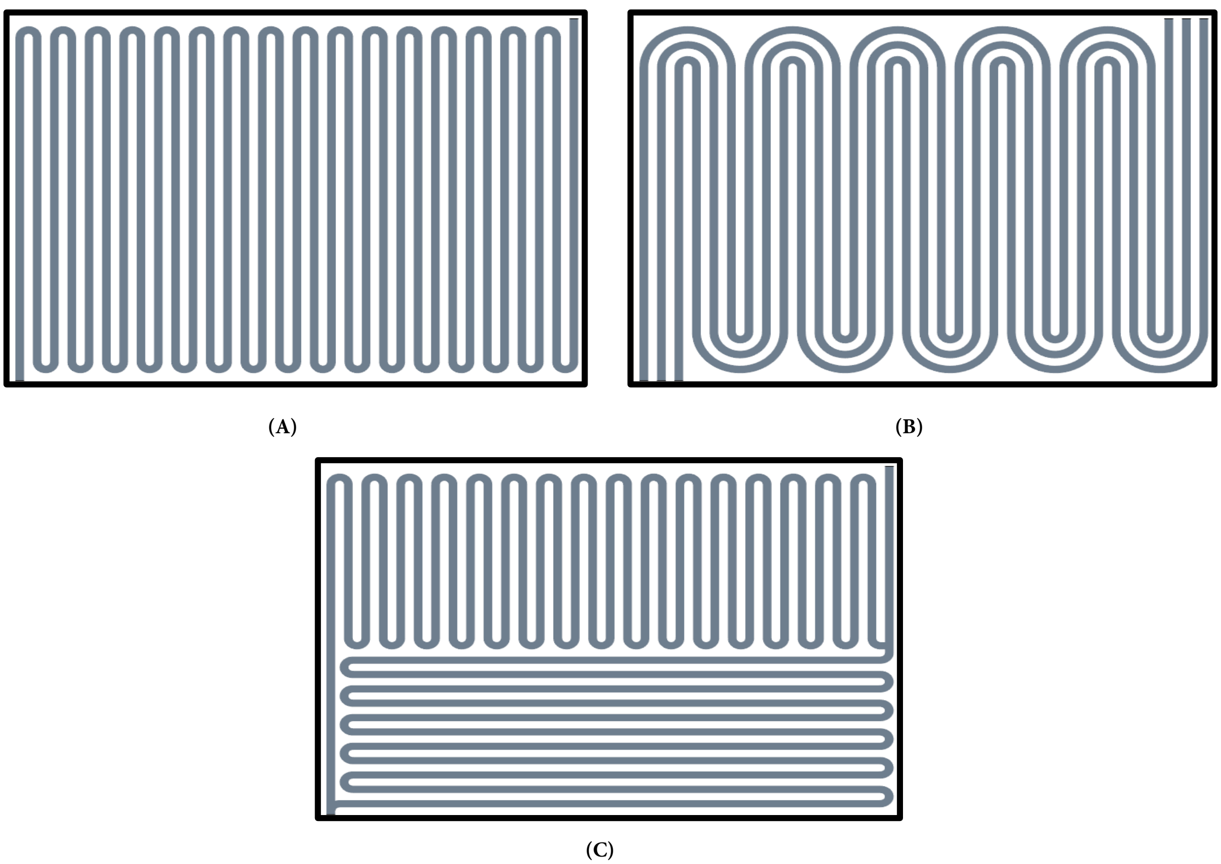

Figure 2. CFD flow field models **(A)** Single Channel Serpentine Flow Field (SCSFF) **(B)** Multi-Channel Serpentine Flow Field (MCSFF) **(C)** Cross-Split Serpentine Flow Field (CSSFF).

3.2 Hydraulic Circuit Analogy Models

The analogy models for the above CAD models have also been developed on the hydraulic circuit concept for a much better understanding of the flow characteristics and resistance phenomenon as shown in Figure 3.

In all the investigated designs, the active area considered is the same with fixed inlet and outlet positions along with 3mm thickness graphite felt electrode ferrous chloride tetrahydrate with the right proportion of 2-mole ammonium. The electrolyte solution contains 3.25-mole ferrous chloride and 0.3-mole ascorbic acid employed in the analysis. Design parameters are formulated based on the dependence of input parameters. The flow field input geometric parameters as mentioned in Table 1. The CSSFF model is considered for future analysis having channel dimensions of width 2mm, depth 2mm, and rib width 2mm over the same active cell area 131cm^2.

3.3. Simulation Methodology

The above model from Figure 2 is set up using commercial engineering software packages. 3D CFD models were imported using Siemens Sim-center STAR-CCM+ tool 15.02.009-R8 (double precision) for simulation, the 3D domain of CSSFF was subjected to meshing and simulations with two different mesh types of polyhedral being unstructured. The trimmer is a hybrid mesh with prisms for near-wall transitions chosen for comparison study as depicted in Figure 4.

Table 1. Flow field configurations geometric parameters

Case	Channel Width mm	Rib Width mm	Channel Depth mm	No of Channels	Active Area cm^2	Channel Hydraulic Diameter mm
SCSFF	2	2	2	33	131	2
MCSFF	2	2	2	33	131	2
CSSFF	2	2	2	44	131	2

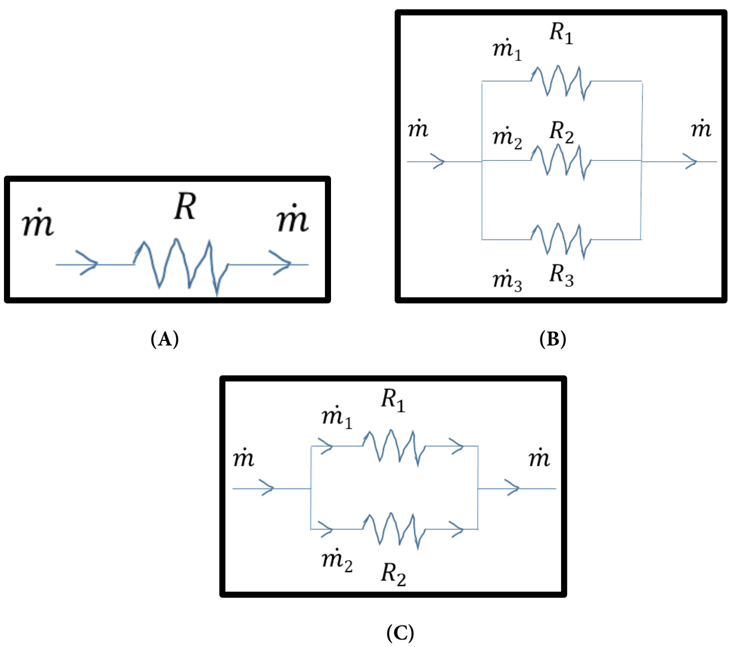

Figure 3. Circuit analogy models **(A)** Single Channel Serpentine Flow Field (SCSFF) **(B)** Multi-Channel Serpentine Flow Field (MCSFF) **(C)** Cross-Split Serpentine Flow Field (CSSFF).

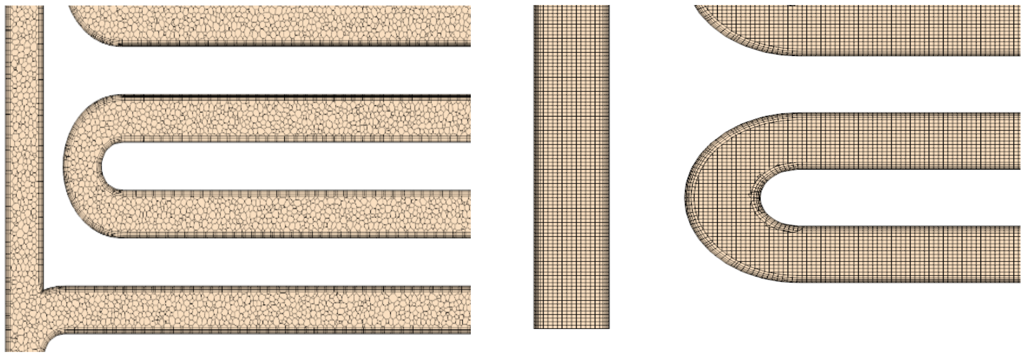

(A) (B)

Figure 4. CSSFF mesh **(A)** Polyhedral **(B)** Trimmer.

The MCSFF model consumes more cells of the order of 3.24 million than the other two models from Table 2 and Table 3.

Medium and fine size mesh is analysed for grid dependency study, medium size mesh has a base size of 0.25mm while fine mesh has 0.125mm. The fine mesh has about 5 times more cells than medium-size mesh which leads to a variation in the results in terms of average velocity. Pressure drop is less than 2% with finer mesh for both polyhedral and trimmer (Table 4).

Therefore, the mesh parameters selected are reasonable and kept constant for this design study. The flow split

Table 2. Mesh cell details for flow field configurations

Variants	SCSFF	MCSFF	CSSFF
Cells (Millions)	3.08	3.24	3.15

Table 3. Mesh cell details for Cross-Split Serpentine Flow Field (CSSFF)

Variants	Polyhedral		Trimmer1	
	Medium Mesh	Fine Mesh	Medium Mesh	Fine Mesh
Cells (Millions)	3.15	14.1	2.3	11.4

Table 4. Grid type observations

Particulars	Polyhedral 1	Polyhedral 2	Trimmer 1	Trimmer 2
Cells Millions	3.15	14.1	2.3	11.4
Pressure Drop (pa)	7135.03	6994.33	6994.45	6864.55
Percentage Change	1.97		2.47	

Table 5. Flow split in CSSFF channels at 150ml/min

Flow Rate ml/min	Mesh Type	Horizontal Channel Flow	Vertical Channel Flow	% of Flow Split Horizontal	% of Flow Split Vertical
150	Polyhedral	4.95	4.05	55	45
	Trimmer	5.04	3.96	56	44

along horizontal and vertical channels in CSSFF is 55% and 45% for polyhedral mesh, whereas for trimmer it is 56% and 44% respectively. The difference is minimal as shown in Table 5.

3.4 Grid Observations

For the same average mesh size or base size polyhedral mesh creates less number of cells as compared to trimmer mesh for complex geometries. Trimmer mesh is more suitable for flows that are aligned to mesh.

Trimmer mesh with incorrect numeric or inappropriate combinations of the calculation parameter can lead to high diffusion and values outside the input range significantly near sharp gradient areas. Polyhedral mesh has the least impact or effect on the type of gradient calculation, method of stability and diffusion. The difference between medium-size mesh and fine-size mesh for both polyhedral and trimmer is very minimal. The cell count and computational time are less for polyhedral mesh which is well acceptable for a trade-off between computational resources and accuracy of solution. As a reason for all the further CFD studies polyhedral mesh was chosen for the simulations.

3.5 Governing Equations

The model for the study is 3D, steady state, laminar incompressible flow.

Mass balance Equation

$$\frac{\partial u}{\partial x} = 0 \tag{1}$$

Linear momentum Equation[37].

$$F = m.\frac{dv}{dt} \tag{2}$$

Pressure drop in the serpentine channel[11].

$$\Delta p = 0.5\rho u^2\left[\frac{4fL}{D} + N_b K_b\right] \tag{3}$$

Here, u average flow velocity through the channel, L straightened length along the channel path and D channel hydraulic diameter, f is the fanning friction factor for a rectangular flow channel, N_b is the number of bends and K_b is the bend loss coefficient for laminar flow regime, where Reynolds's number is between 100<*Re*<1000.

Momentum conservation Equation

for flow through porous substrate.

$$\rho\left(\frac{du}{dt}\right) = \rho g - \frac{\partial p}{\partial x} + \mu\nabla^2 u + S_m \tag{4}$$

Pressure drop in the porous substrate is determined by source term Equation[38].

$$S_m = \frac{\Delta p}{L} = \alpha V + \beta V^2 \tag{5}$$

The source term is the additional term added to the momentum equation to determine the viscous and inertial effects, which results in flow resistivity in a porous substrate. i.e.,αV is Darcy's equation, where viscous effects are predominant. ii.e.squared is βV^2 is a forchheimer equation, where inertial effects are predominant.

$$\therefore \frac{\Delta_p}{L} = \sigma, \quad \alpha = {}^{\mu}/_{k}, \quad \beta = 2.88\times 10^{-6}\frac{\tau}{\epsilon k} \tag{6}$$

Tamayol- Bahrami model for permeability[30]

$$\frac{k}{d^2} = 0.012(1-\phi)\left[\frac{\pi}{4\phi^2} - 2\frac{\pi}{4\phi} + 1\right]\left[1 + \frac{0.72\phi}{(0.89-\phi)^{0.54}}\right] \tag{7}$$

$$\therefore i.e., \qquad \tau = 1 + 0.72\frac{1-\epsilon}{(\epsilon-0.11)^{0.54}} \tag{8}$$

$$\therefore i.e., \qquad \tau = \left(\frac{1}{\epsilon}\right)^{0.5} or \left(\frac{1}{1-\phi}\right)^{0.5} \tag{9}$$

$$\therefore i.e., \qquad \phi = 1-\epsilon, \qquad \epsilon_0 = 1-\frac{\rho_b}{\rho_f} \tag{10}$$

$$\therefore i.e., \qquad \epsilon_c = 1-\frac{(1-\epsilon_0)t_0}{t_c} \tag{11}$$

Compression ratio

$$CR = 1-\frac{t_c}{t_0} \tag{12}$$

Evaluating flow distribution through the electrode volume by Equations (13) and (14) are available from Sim centre STAR-CCM+ user guide v1502009-r8.

Surface uniformity index

$$\emptyset = 1-\frac{\sum_f \left[\emptyset_{f-}\emptyset\right]A_f}{2[\emptyset]\sum_f A_f} \tag{13}$$

Volume uniformity index

$$\emptyset = 1-\frac{\sum_c [v_{c-}v]Vc}{2[v]\sum_c Vc} \tag{14}$$

Volume weighted average of planar velocity[38]

$$v_{ph} = \frac{\sqrt{v_x^2+v_y^2}}{\varepsilon} v_{ph} = \frac{1}{v}\int_v^1 v_{ph} dv \tag{15}$$

4.0 Results and Discussion

The progress of the converging CFD solution is observed besides the residuals via the pressure loss over the cell channel between the inlet and outlet of the domain. After about approximately 600 iterations, convergence is assumed, with not much significant change in the physical values as depicted in Figure 5. A residual level of 1.0e-04 is targeted for all field variables and asymptotic behavior in pressure drop with iterations is desired as depicted in Figure 6. The quality and values of desired quantities seem to be physical and acceptable.

For benchmarking and validation of the CFD software chosen for numerical study i.e., Sim centre STARCCM+, a suitable literature with experimental results was selected. The geometry was constructed to match the dimensions utilised from article[39], Figure 7(B). The grid dependency studies and numerical simulations were carried out for various Reynolds numbers. For validation purposes, Reynolds number (Re) 116 with peak flow velocity is about 0.4m/s at the inner wall at 0° of the bend and a lower velocity of about 0.1m/s from Figure 7(A). At 180° of bend, the simulation results showed an opposite behaviour as compared to the flow profile at 0° from Figure 7(B). Similar results were obtained in measurement[35].

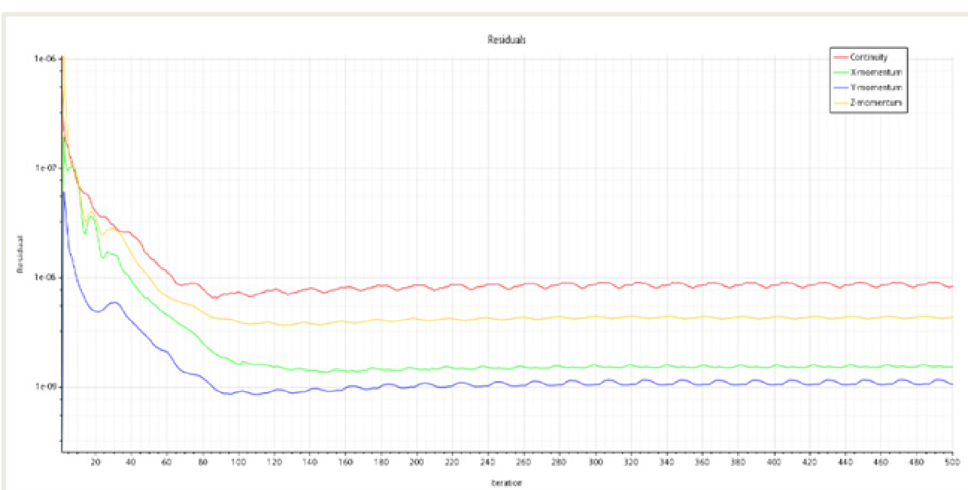

Figure 5. Residual versus iterations plot.

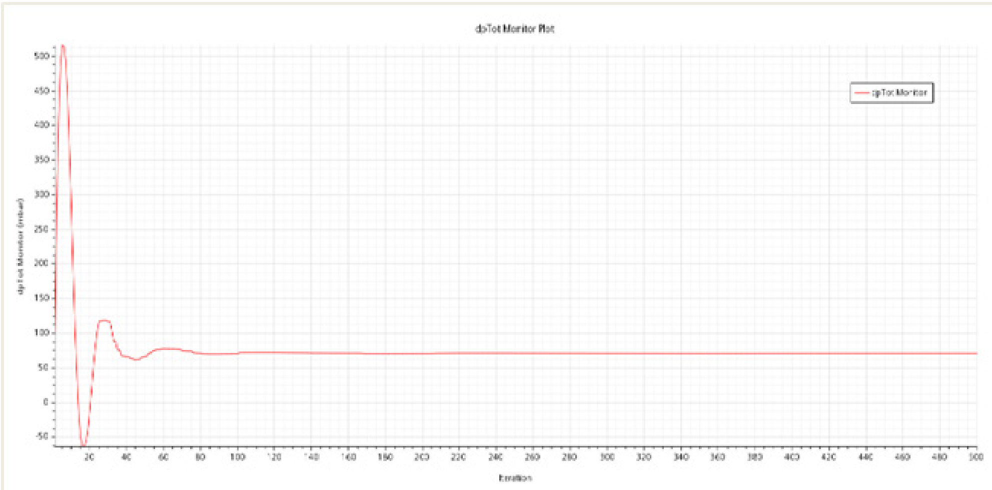

Figure 6. Pressure drop versus iterations plot.

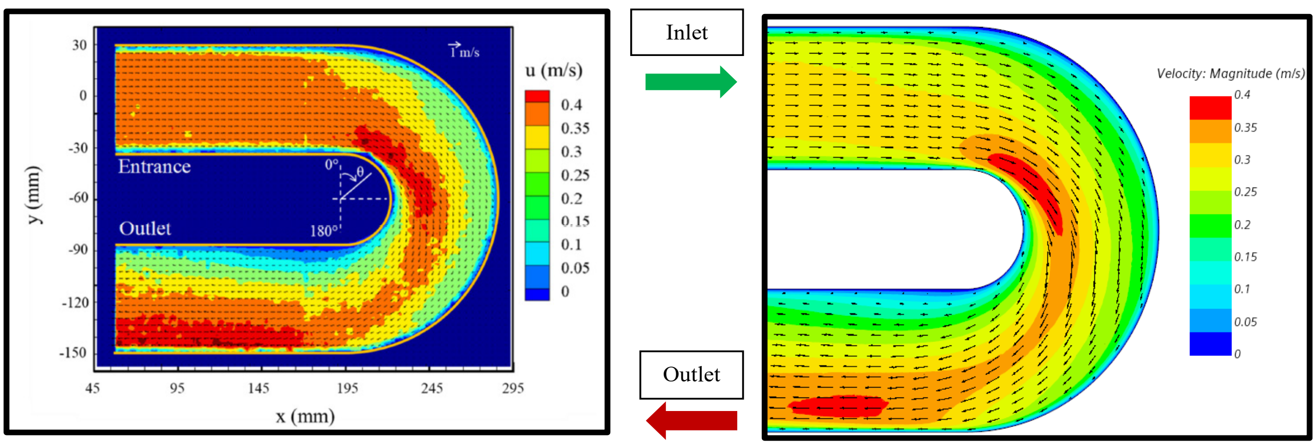

(A) **(B)**

Figure 7. **(A)** and **(B)** Rectangular curved duct actual measurement value and CFD simulation value.

4.1 Mesh Independence Study Result

To get the right discretisation applicable for the physics and geometry of interest CSSFF, a grid independence study was carried out to ensure the correct grid sizes. numerical simulations were carried out with 3-dimensional CFD commercial code.

The initial mesh was generated based on global Reynolds numbers, the hydraulic diameter of the channels, near-wall resolutions, and the transition between near-wall mesh and core mesh. A few sets of grid sizes such as ultra-fine, fine, medium, coarse and very coarse mesh sizes were evaluated with pressure drop and maximum velocity was compared across various sizes to check grid dependence as shown in Table 6.

The variation in pressure drop across the mesh sizes was less than 2% and velocity value variation was less than 0.5% as shown in Figure 8. The theory states that a denser mesh is preferred for a numerical simulation but results in higher computational time. As a compromise

Table 6. Comparison of mesh sizes with flow physics

Particulars	Ultra-Fine Mesh	Fine Mesh	Medium Mesh	Coarse Mesh	Very Coarse Mesh
Base Size mm	0.125	0.1875	0.25	0.3125	0.5
Pressure Drop Pa	6930.1	7019.8	7050.2	7048.9	7060.9
Max Velocity m/s	0.88	0.87	0.87	0.86	0.85
Cell Counts Millions	17.7	7	3.5	2.3	0.82
Pressure Drop Variation %	1.30851	0.0309	0.40218	0.38333	0.5539

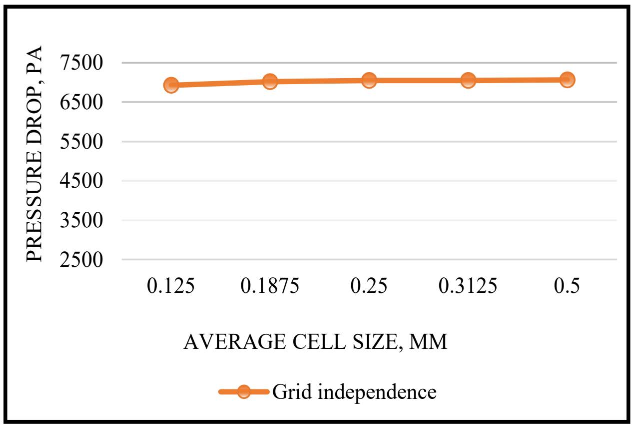

(A)

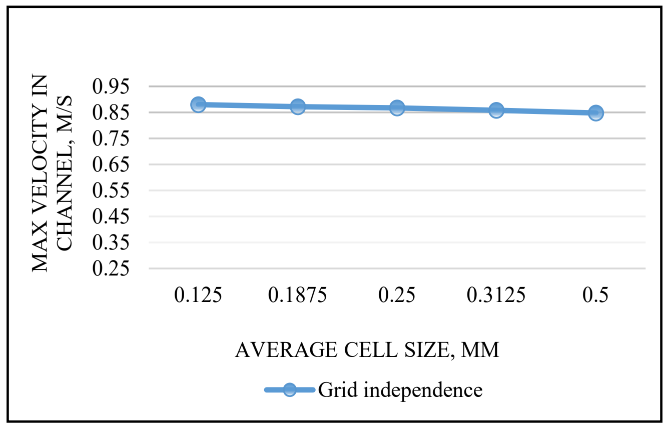

(B)

Figure 8. **(A)** and **(B)** Average cell size versus pressure drop (and max velocity of fluid flow.

between accuracy and computational time, medium size mesh 0.25mm average size with a minimum of 5 prism layers for near wall resolution and transition is considered for all further studies and simulations.

4.2 Simulation Results

4.2.1 Flow Field Configurations

CFD-based results are presented here, considering the CSSFF design parameters from Table 1. Flow velocity magnitude through the CSSFF channel for polyhedral and trimmer mesh types at a volumetric flow rate of 150ml/min, with geometric details as shown in Table 1 and simulated image in Figure 9. The result demonstrates that trimmer mesh shows two primary and two secondary vortices while polyhedral mesh shows two large vortices. As can be seen from Figure 9(A), polyhedral mesh for CSSFF at 150ml/min shows that velocity distribution at the domain inlet is high at the centre of the channel and reduces gradually towards the wall as it flows inward. Flow split, results in the fluid particle velocity retardation at the entrance to horizontal and vertical channels leading to the vortices with flow disturbance, whereas, in subsequent channels, the flow gets stabilised with minimum velocity magnitude and smooth flow towards the outlet. Thus the trimmer mesh Figure 9(B) shows slight instability in the flow pattern at the channel bends with higher flow velocity as compared to polyhedral mesh at the same flow rate. The velocity of 0.510m/s and 899 Reynold's number still the flow exhibits a laminar nature Table 7.

Reynolds number (Re) characterises the flow regime. The critical Reynolds number for duct/channel flows is 2300. Re < 2300 is laminar flow, and Re > 2300 is turbulent

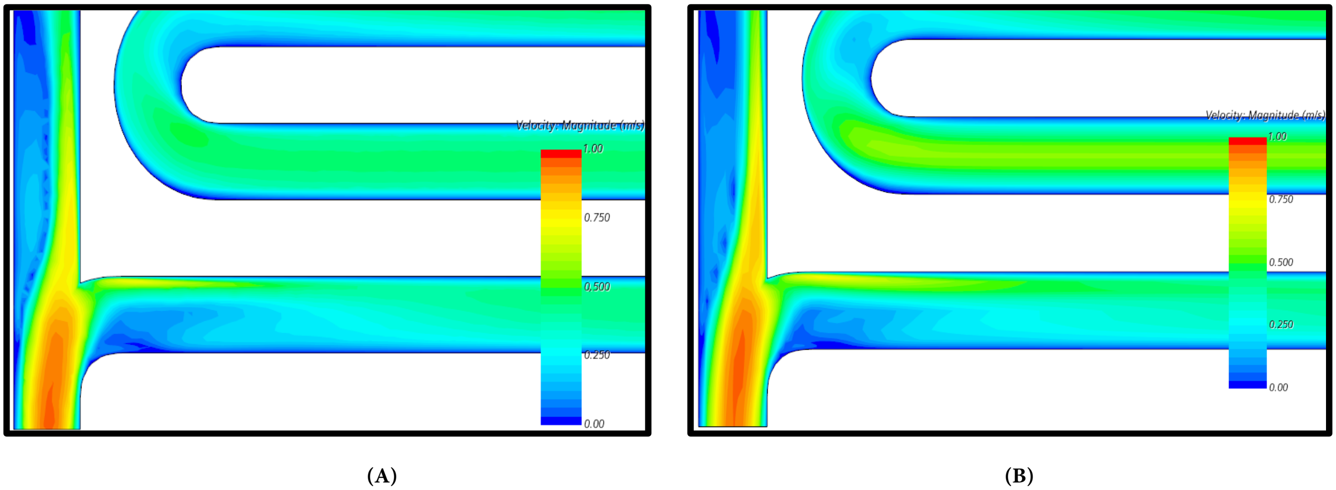

Figure 9. Velocity magnitude for CSSFF at 150ml/min **(A)** Polyhedral mesh **(B)** Trimmer mesh.

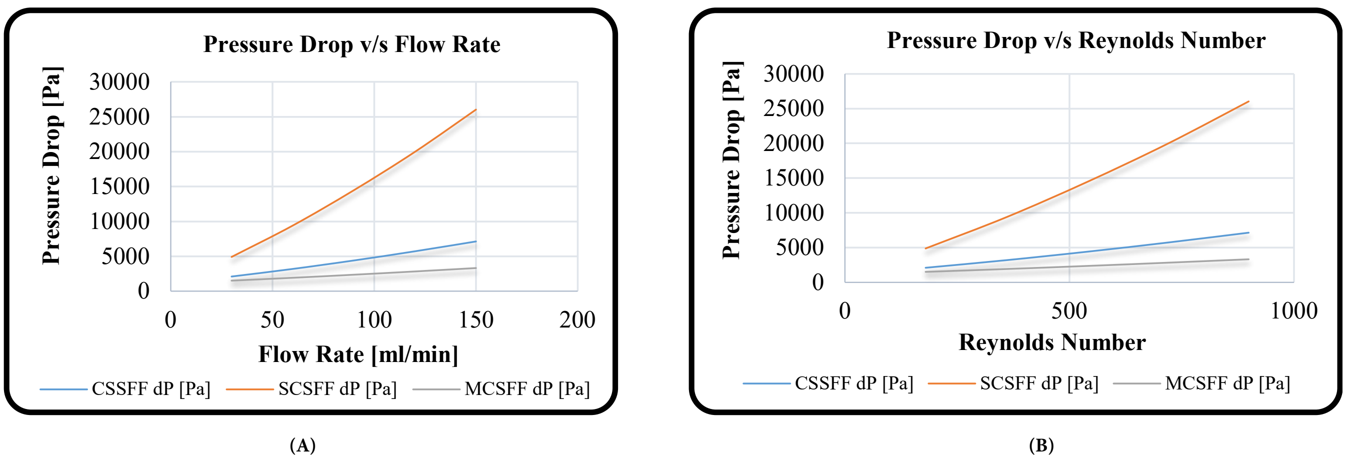

Figure 10. **(A)** and **(B)** Pressure drop versus flow rate and Reynolds's number for flow field configuration.

flow. Figure 10(A) and (B) illustrate graphically the linear variation of pressure drop for various flow rates, and Reynolds's number for different flow field configurations. The maximum pressure drops of 26046.32 Pa for SCSFF at Re number 899 varies linearly. Very similar patterns were observed over the other two configurations with reduced pressure drop values operating at the same conditions.

The flow velocity magnitude contours for different flow field configurations. Figure 11 demonstrates minimum velocity and uniform flow exist in MCSFF. Figure 11(B) shows the domain inlet to outlet compared to the other two flow fields. Thus in SCSFF (Figure 11(A)), the flow velocity distribution is slightly higher through the straight length of the channel and reduces towards the bends over all subsequent channels. CSSFF (Figure 11(C)) shows that the flow of velocity is maximum at the inlet and outlet of the domain and also at the channel split and convergence point. Whereas, the flow of velocity is slightly higher through horizontal channels and reduces gradually through the vertical channels with uniform flow through the entire flow field.

Pressure distribution is a significant parameter in regulating cell performance. As per Figure 12(A) SCSFF, the fluid pressure at the inlet is maximum, more than the

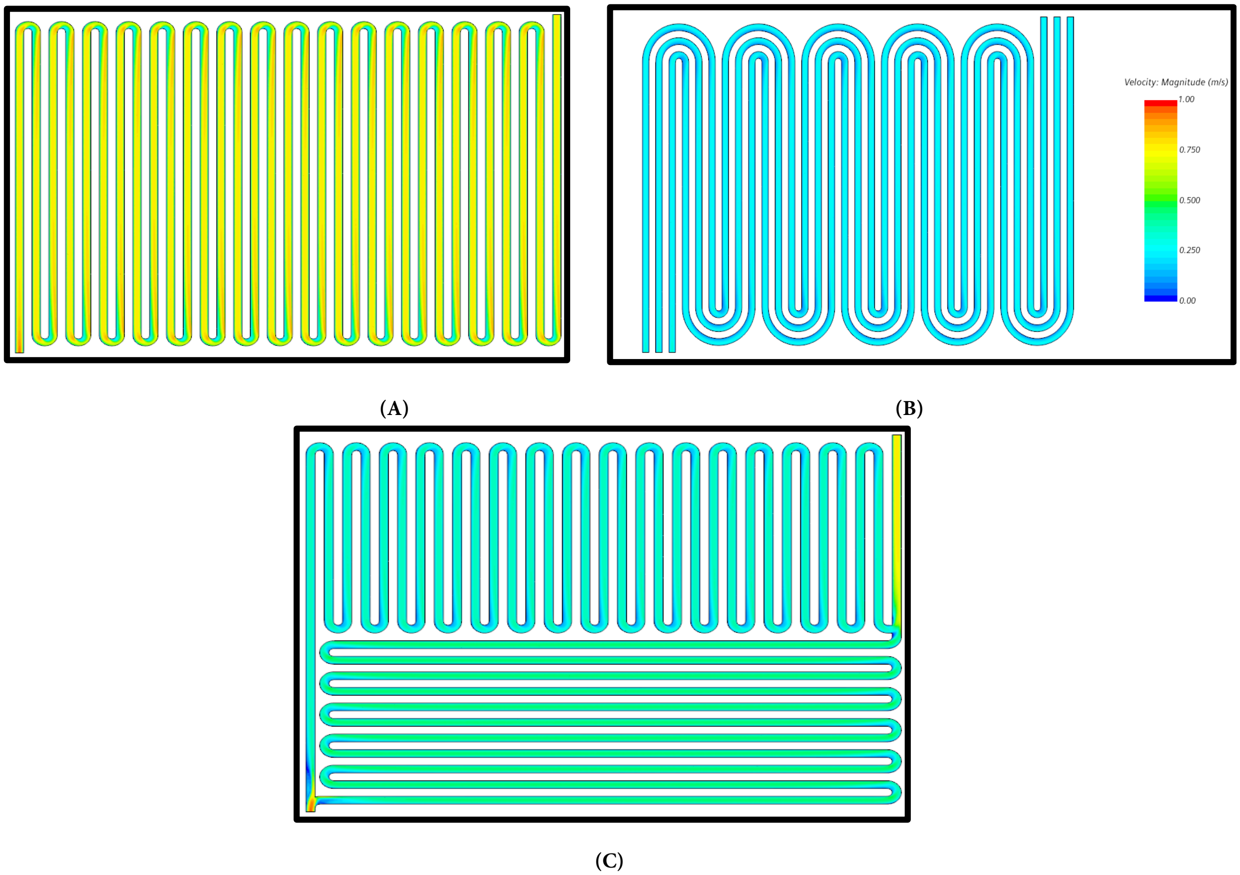

Figure 11. Velocity distribution at 150ml/min **(A)** SCSFF **(B)** MCSFF **(C)** CSSFF.

Table 7. Pressure drop values for flow field configuration at various flow rates, velocity and Reynolds's number

Flow Rate ml/min	Velocity m/s	Reynold's Number (Re)	Pressure Drop (Pa)		
			SCSFF	MCSFF	CSSFF
30	0.102	180	4897.82	1526.00	2084.56
60	0.204	360	9395.60	1927.61	3177.10
90	0.306	540	14465.87	2363.00	4394.58
120	0.408	720	19977.76	2824.00	5716.06
150	0.510	899	26046.32	3307.00	7135.03

order of 25000 Pa and shows a gradual drop in pressure for subsequent channels with a minimum pressure of the order less than 100 Pa. Figure 12(B) MCSFF shows that pressure distribution is maximum to the order of 3000 Pa, but much less than the above flow design. The flow gets distributed equally along all three channels at the inlet, thereby reducing the pressure drop. In Figure 12(C) CSSFF, the pressure gradient is slightly higher at the inlet compared to MCSFF but much less than SCSFF. Whereas, from Table 7, we observe the least pressure drop values for MCSFF flow configuration for all the flow rates and Reynolds's number.

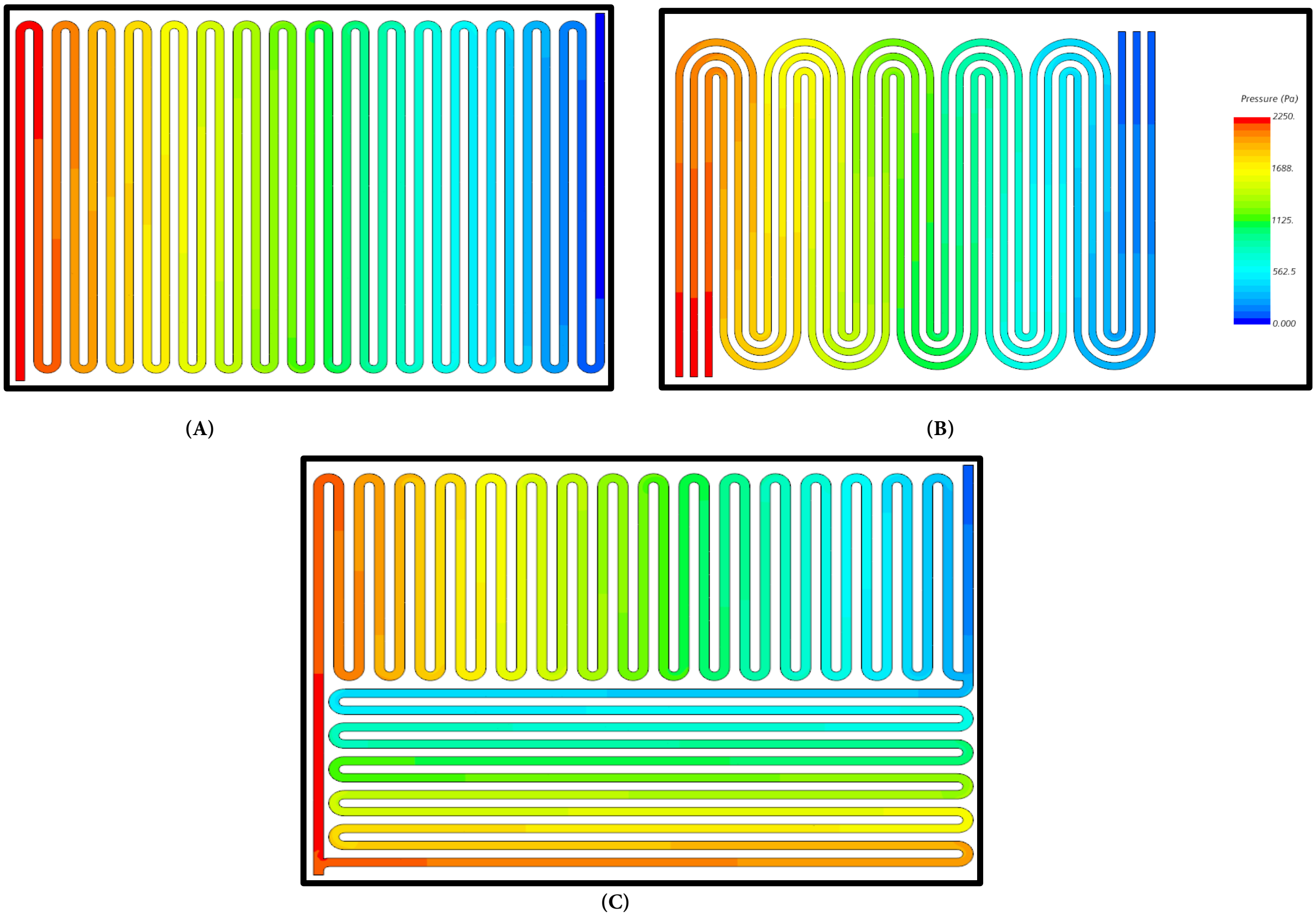

Figure 12. Pressure distribution at 150ml/min **(A)** SCSFF **(B)** MCSFF **(C)** CSSFF.

4.2.2 Flow Field along with Porous Substrate Configurations

For the models simulated as shown in Figure 13, the felt volume uniformity index of velocity magnitude amounts to 69% at a compression ratio of 50%. The porous electrode felt intrusion values are around 20%–25% which is well evaluated[10] from Table 8. Simulated results demonstrate quite realistically, the increase in compression effect on the assembly (flow channel + electrode) which accounts for a linear increase in pressure drop and flow resistivity seen from the surface and volume uniformity index (Table 8, Figure 13(B)) i.e., CR 50% flow distribution velocity is maximum at the mid-height of the plane and slightly non-uniform flow over some regions in horizontal flow field channel (stagnant). We can also witness reduced velocity flow and uniform flow distribution over most of the regions in vertical and some regions of horizontal channels have improved fluid dispersion rate and wet ability resulting in optimal reactant species transport through the electrode plane which has enhanced electrochemical activity. Similar flow distribution and velocity patterns were observed at CR 60% and CR 70%. The more stagnant regions over the horizontal plane and high-velocity rate cause increased flow resistance, pressure drop and non-uniform flow distribution which may contribute to a drop in cell performance and lead to variation in operating parameters such as Discharge Power Density (DPD), Depth of Discharge (DoD) and Energy Density (ED). The observations of Table 8 data demonstrates the linear increment of the pressure drop value from CR 50% to CR 70% and it is almost approximated to increase by 1.5 times. Similar changes were also observed in the uniform flow distribution index for velocity magnitude over the

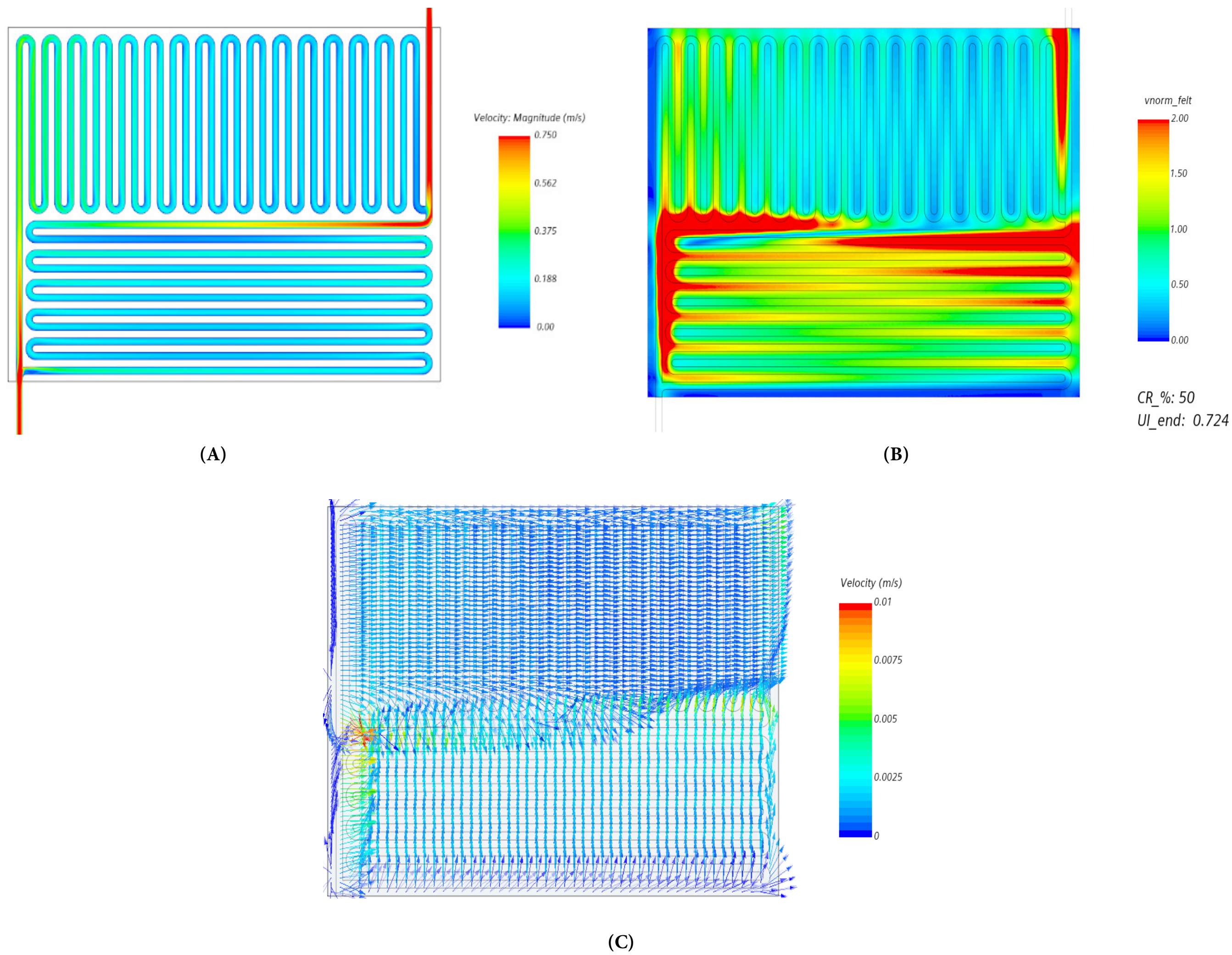

Figure 13. (**A**), (**B**), and (**C**), CSSFF channel mid-plane velocity magnitude profile, graphite electrode felt end plane flow distribution profile at CR 50%, and Graphite electrode felt end plane velocity profile

Table 8. Numerically determined pressure drop value and uniformity index at mid and end surface of graphite electrode felt for different Compression Ratios (CR) for Cross-Split Serpentine Flow Field (CSSFF) at 150ml/min

Particulars	CR 50%	CR 60%	CR 70%
Pressure Drop pa	7347.6	9292.0	12750.0
Surface Uniformity Index-Mid	71.3	69.3	66.6
Surface Uniformity Index-End	72.4	70.2	67.4
Volume Uniformity Index-Felt	69.0	67.0	64.3

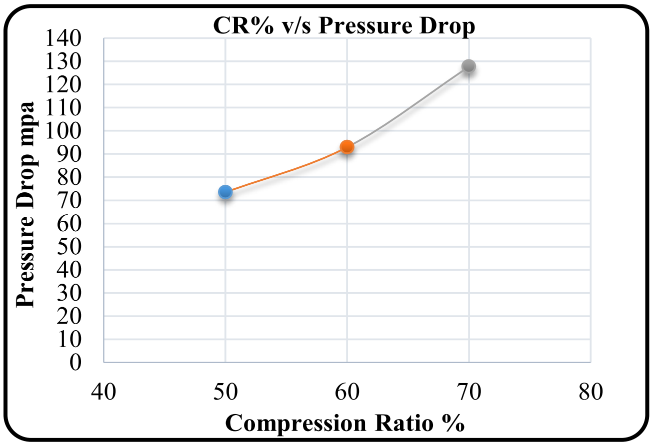

(A)

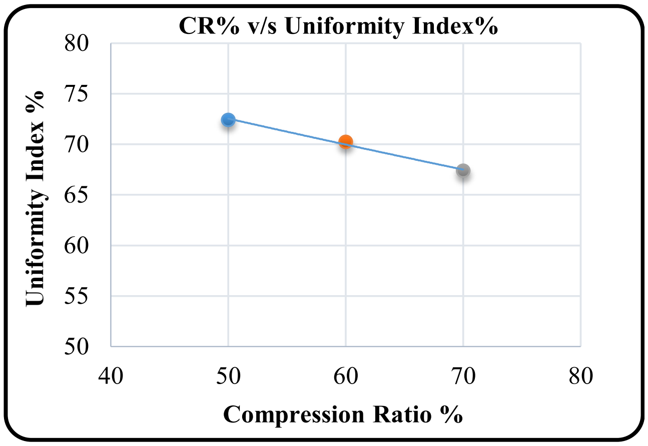

(B)

Figure 14. **(A)**, and **(B)**, Compression ratio versus pressure drop and compression ratio versus surface uniformity index end plane for CSSFF.

surface and volume of the end planes i.e., 72.4. 69 shows highest for CR 50% and gradually decreases for CR 70% i.e., 67.4, and 64.3.

Graph representing compression ratio that is directly proportional to pressure drop and inversely proportional to uniformity index from Figure 14 (A), and (B).

5.0 Conclusion

The consideration of different flow field configuration designs such as SCSFF, MCSFF and CSSFF with the same geometrical dimensions i.e., channel, rib width and channel depth from Table 1 and active cell area of 131cm^2 were subjected to various operating conditions such as flow rates, Reynold's number and compression ratios to determine and systematically evaluate the system parameters such as Pressure Drop , velocity magnitude, fluid flow uniformity index i.e., for surface and volume through the channel and porous electrode substrate plane

- The CFD model of CSSFF was found to be the key analysis to achieve the expected value for every defined system parameter and was satisfied with the excepted pressure drop at a reasonably, agreeable value with the least influence on remaining parameters.
- Models were subjected to polyhedral and trimmer mesh types with fine mesh having about 5 times more cells than medium size. The variation of results in terms of average velocity and pressure drop was less than 2% with finer mesh for both the mesh types (Table 4).
- Flow split along horizontal and vertical channels of CSSFF models for both the mesh types shows much better fluid flow through the channels at maximum flow rate resulting high distribution rate (Table 5).
- The cell count and computational time are less for polyhedral mesh which is well acceptable for a trade-off between computational resources and the accuracy of the solution.
- The CSSFF configurations with flow rate of 150ml/min, Reynold's number 899, was 7135.03 Pa which is 1.5 times greater than for MCSFF and 3.5 times lesser than the SCSFF model tabulated in Table 7. CSSFF design agrees optimally with other flow field designs and operating parameters.
- CSSFF along with porous substrate (graphite felt electrode) at compression ratios 50%, results in optimal values of pressure drop , surface and volume uniformity index across the cell active area operating at a maximum flow rate of 150ml/min from Table 8.

- CSSFF along with porous substrate (graphite felt electrode) at CR 50%, demonstrates reduced flow resistance, operational cost and pumping energy and provides optimal permeability to improve flow distribution and enhance electrochemical activity compared to other CR ratios.

Hence, the above component assembly may be recommended to be installed in all IRFBs to improve the cell performance. If we look closely the pressure drop value flow through CSSFF channels accounts for 7135.03Pa and with the porous electrode configuration accounts for 7347.6Pa at the same flow rate of 150ml/min over a defined active cell area, a slight increase is witnessed, which have rightly justified our numerical analysis. A lesser pressure gradient across the active cell area reduces the pumping power and increases flow uniformity with high reactant species concentration, discharge power density, and depth of discharge. The above-described method and approach from this extensive study can be suitably applied to different flow field geometries, designs, cell sizes, electrodes, electrolytes and any type of RFB systems.

This flow field configuration shows a positive sign that it may be an excellent choice for an IRFB, operating at defined parameters to enhance its renewable energy storage capacity and depth of discharge efficiently. Henceforth, this could significantly raise the concern about equipping this storage system as an off-grid power auxiliary supply module for seamless mine operations in mining and mineral processing industries effectively.

6.0 Acknowledgement

The authors gratefully thank the Jyothy Institute of Technology for the facilities provided to conduct the research work.

7.0 References

1. Zhengqui Y, Jianlu Z, Michael CW, Kintner-Meyer, Xiaochuan L, Daiwon C, John P, Lemmon, Jun L. Electrochemical energy storage for the green grid. Chemical Reviews: ACS Publications. 2011; 111:3577-613. https://doi.org/10.1021/cr100290v. PMid:21375330.
2. Zhenguo Y, Yun L, Suresh B, Carl H I, Jamie DH. Enabling renewable energy and future grid - with advanced electricity storage. Energy Storage Technologies. 2010; 62:14-23. https://doi.org/10.1007/s11837-010-0129-0.
3. Piergiorgio A, Massimo G, Federico M. Redox flow batteries for the storage of renewable energy: A review. Renewable and Sustainable Energy Reviews. 2014; 29:325-35. https://doi.org/10.1016/j.rser.2013.08.001.
4. Narendra MK, Manoj Kumar S, Vijayakumar GC, Kadirgama K, Samykano M, Krishna Venkatesh, Murlidhara HB. Effect of flow field geometry on hydrodynamics of flow in redox flow battery. Energy Engineering, Tech Science Press. 2022; 119:201-17. https://doi.org/10.32604/EE.2022.016597.
5. Luis FA, Carlos Ponce de León, Frank Walsh C. Redox flow batteries for energy storage: Their promise, achievements and challenges. Current Opinion in Electrochemistry. 2019; 16:117-26. https://doi.org/10.1016/j.coelec.2019.05.007.
6. Bruce D, Haresh K, Jean-Marie T. Electrical energy storage for the grid: A battery of choices. Materials for grid energy. Science AAAS. 2011; 334(6058):928-35. https://doi.org/10.1126/science.1212741. PMid:22096188.
7. Arenas LF, Ponce de León C, Walsh FC. Engineering aspects of the design, construction and performance of modular redox flow batteries for energy storage. Journal of Energy Storage. 2017; 11:119-53. https://doi.org/10.1016/j.est.2017.02.007.
8. Skyllas-Kazacos M, Chakrabarti MH, Hajimolana SA, Mjalli FS, Saleem M. Progress in flow battery research and development. Journal of the Electrochemical Society. 2011; 158(8):55-79. https://doi.org/10.1149/1.3599565.
9. Michael Gerhardt R, Andrew Wong A, Michael JA. The effect of interdigitated channel and land dimensions on flow cell performance. Journal of the Electrochemical Society. 2018; 165(11):2625-43. https://doi.org/10.1149/2.0471811jes.
10. Kumar S, Jayanti S. Effect of electrode intrusion on pressure drop and electrochemical performance of an all-vanadium redox flow battery. Journal of Power Sources. 2017; 360: 548-58. https://doi.org/10.1016/j.jpowsour.2017.06.045.

11. Gundlapalli R, Jayanti S. Effect of channel dimensions of serpentine flow fields on the performance of a vanadium redox flow battery. Journal of Energy Storage. 2019; 23:148-58. https://doi.org/10.1016/j.est.2019.03.014.
12. Kumar S, Jayanti S. Effect of flow field on the performance of an all-vanadium redox flow battery. Journal of Power Sources. 2016; 307:782-87. https://doi.org/10.1016/j.jpowsour.2016.01.048.
13. Gundlapalli R, Jayanti S. Effective splitting of serpentine flow field for applications in large-scale flow batteries. Journal of Power Sources. 2021; 487:229409. https://doi.org/10.1016/j.jpowsour.2020.229409.
14. T Jyothi L, Jayanti S. Ex-situ experimental studies on serpentine flow field design for redox flow battery systems. Journal of Power Sources. 2014; 248:140-6. https://doi.org/10.1016/j.jpowsour.2013.09.084.
15. Maharudrayya S, Jayanti S, Deshpande AP. Flow distribution and pressure drop in parallel-channel configurations of planar fuel cells. Journal of Power Sources. 2005; 144:94-106. https://doi.org/10.1016/j.jpowsour.2004.12.018.
16. T. Jyothi L, Jayanti S. Hydrodynamic analysis of flow fields for redox flow battery applications. Journal of Applied Electrochemistry. 2014; 44:995-1006. https://doi.org/10.1007/s10800-014-0720-0.
17. S. Kumara T, Jyothi L, Jayanti S. Experimental studies of permeability measurement and hydrodynamics study of all-vanadium redox flow battery. Materials Today: Proceedings. 2018; 5:23169-76. https://doi.org/10.1016/j.matpr.2018.11.048.
18. Dennison CR, Ertan Agar, Bilen Akuzum, Kumbura EC. Enhancing mass transport in redox flow batteries by tailoring flow field and electrode design. Journal of the Electrochemical Society. 2016; 163(1):5163-69. https://doi.org/10.1149/2.0231601jes.
19. Xu Q, Zhao TS, Leung PK. Numerical investigations of flow field designs for vanadium redox flow batteries. Applied Energy. 2013; 105:47-56. https://doi.org/10.1016/j.apenergy.2012.12.041.
20. Rober JK, Pavan K, Kevin W, Mark P. A generalized model of the flow distribution in channel networks of planar fuel cells. Journal of Power Sources. 2002; 109(1):148-59. https://doi.org/10.1016/S0378-7753(02)00090-3.
21. Xianguo L, Imran S. Review of bipolar plates in PEM fuel cells: Flow-field designs. International Journal of Hydrogen Energy. 2005; 30(4):359-71. https://doi.org/10.1016/j.ijhydene.2004.09.019.
22. Bo-Ra K, Deok-Young S, Yun-Ho C, Yong-Hee L. A study on flow characteristics and flow uniformity for the efficient design of a flow frame in a redox flow battery. Applied Sciences MDPI. 2020; 10:929. https://doi.org/10.3390/app10030929.
23. Gundlapalli R, Jayanti S. Performance characteristics of several variants of interdigitated flow fields for flow battery applications. Journal of Power Sources. 2020; 467:228225. https://doi.org/10.1016/j.jpowsour.2020.228225.
24. Xu Q, Zhao TS, Zhang C. Performance of a vanadium redox flow battery with and without flow field. Electrochimica Acta. 2014; 142:61-7. https://doi.org/10.1016/j.electacta.2014.07.059.
25. Maharudrayya S, Jayanti S, Deshpande AP. Pressure losses in laminar flow through serpentine channels in fuel cell stacks. Journal of Power Sources. 2004; 38:1-13. https://doi.org/10.1016/j.jpowsour.2004.06.025.
26. Xinyou K, Joseph MP, J. Iwan D, Alexander, Robert FS. Redox flow batteries with serpentine flow fields: Distributions of electrolyte flow reactant penetration into the porous carbon electrodes and effects on performance. Journal of Power Sources. 2018; 384:295-302. https://doi.org/10.1016/j.jpowsour.2018.03.001.
27. Xinyou K, Joseph M.P, J. Iwan D, Alexander, Jesse SW, Thomas Zawodzinski A, Robert FS. Rechargeable redox flow batteries: Flow fields, stacks and design considerations. Chemical Society Reviews. 2018; 47(23):8721-43. https://doi.org/10.1039/C8CS00072G. PMid:30298880.
28. Prumbohm E, Becker M, Flaischlen S, Wehinger GD, Turek T. Flow field designs developed by comprehensive CFD model decrease system costs of vanadium redox-flow batteries. Journal of Flow Chemistry. 2021; 11:461-81. https://doi.org/10.1007/s41981-021-00165-2.
29. Qiong Z, Feng X, Xianfeng L, Guiling N, Huamin Z. Flow field design and optimisation based on the mass transport polarisation regulation in a flow-through type vanadium flow battery. Journal of Power

Sources. 2016; 324:402-11. https://doi.org/10.1016/j.jpowsour.2016.05.110.
30. Heledd J, Natalia Y. Corporate social responsibility in the mining industry: Exploring trends in social and environmental disclosure. Journal of Cleaner Production. 2006; 14:271-84. https://doi.org/10.1016/j.jclepro.2004.10.004.
31. Norgate T, Haque N. Energy and greenhouse gas impacts of mining and mineral processing operations. Journal of Cleaner Production. 2010; 18:266-74. https://doi.org/10.1016/j.jclepro.2009.09.020.
32. Michelle L, Dean M, Jacek P. Energy and mining e the home truths. Journal of Cleaner Production. 2014; 1:1-23.
33. Tsisilile I, Kwame A, Alexandra N, Travis L, Jill EC. Integrating renewable energy into mining operations: Opportunities, challenges, and enabling approaches. Applied Energy. 2021; 300:117375. https://doi.org/10.1016/j.apenergy.2021.117375.
34. Tamayol A, McGregor, Bahrami FM. Single phase through-plane permeability of carbon paper gas diffusion layers. Journal of Power Sources. 2012; 204:94-9. https://doi.org/10.1016/j.jpowsour.2011.11.084.
35. Anarghya D, Anantha MS, Venkatesh K, Santosh MS, Geetha Priya M, Muralidhara HB. Bermuda grass-derived nitrogen-doped carbon as electrocatalyst in graphite felt electrode to increase the efficiency of alliron redox flow batteries. Journal of Electroanalytical Chemistry. 2020; 878:114577. https://doi.org/10.1016/j.jelechem.2020.114577.
36. Tenhumberg. Kinetic studies at carbon felt electrodes for vanadium redox-flow batteries under controller transfer current density conditions. Electrochim Acta. 2017; 252:12-24. https://doi.org/10.1016/j.electacta.2017.07.062.
37. White FM. Fluid Mechanics. McGraw Hill.Inc, University of Rhode Island; 1994.
38. Bortolin S, Toninelli P, Maggiolo D, Guarnieri M, Del Col D. CFD study on electrolyte distribution in redox flow batteries. Journal of Physics: Heat transfer Conference. 2015; 655:012049. https://doi.org/10.1088/1742-6596/655/1/012049.
39. Afshin G, Peter R. PIV-Measurements of centrifugal instabilities in a rectangular curved duct with a small aspect ratio. Fluids, MDPI. 2021; 6(5):184. https://doi.org/10.3390/fluids6050184.

Nomenclature :

IRFB	Iron Redox Flow Battery
CSSFF	Cross-Split Separation Flow Fluid
CR	Compression Ratio
D	Hydraulic diameter of the channel (m)
d	Fiber diameter (m)
f	Fanning friction factor
k	Perabity (m^2)
Kb	Bend loss co-efficient
M	Moles
MCSFF	Multi-Channel Separation Flow Fluid
Nb	Number of bends
Δp	Pressure drop (Pa)
Q	Volumetric flow rae (ml/min)
u	Average velocity(m/s)
S_m	Source term
SCSFF	Single-Channel Separation Flow Fluid
t	Thickness of the electrode (m)
V	Mean velocity (m/s)

v_{in}	Inlet velocity (m/s)
v_{out}	Outlet velocity (m/s)
v_{pv}	Volume-weighted average of planar velocity
vc	local velocity magnitude

Greek Symbols:

μ	Dynamic viscosity of electrolyte (PaS)
α	Viscosity coefficient
β	Inertial resistance coefficient
σ	Shear stress(N/m^2)
ϵ	Porosity
ϕ	Solid volume fraction =(1-ϵ)
τ	Tortuosity factor
ρ_b&ρ_f	Package and fibre nsity (kg/m^3)
Ø	Surface and volume uniformity index

Subscripts:

c	Compression
o	Original (uncompressed)